Energy Storage Materials 37 (2021) 345–353

Contents lists available at ScienceDirect

Energy Storage Materials

journal homepage: www.elsevier.com/locate/ensm

Lattice-resolution visualization of anisotropic sodiation degrees and revelation of sodium storage mechanisms in todorokite-type MnO_2 with *in-situ* TEM

Ran Cai[a,1], Shiying Guo[b,1], Yi Wu[a,1], Shengli Zhang[b], Yuanwei Sun[c], Shulin Chen[c], Peng Gao[c,*], Chongyang Zhu[a], Jing Chen[d], Zhen Zhu[d], Litao Sun[a,*], Feng Xu[a,*]

[a] SEU-FEI Nano-Pico Center, Key Laboratory of MEMS of Ministry of Education, Southeast University, Nanjing 210096, China
[b] College of Materials Science and Engineering, Nanjing University of Science and Technology, Nanjing 210094, China
[c] Electron Microscopy Laboratory, and International Centre for Quantum Materials, School of Physics, Peking University, Beijing 100871, China
[d] School of Electronic Science and Engineering, Southeast University, Nanjing 210096, China

ARTICLE INFO

Keywords:
Todorokite-type MnO_2
Lattice-resolution
In-situ transmission electron microscopy
Sodium storage mechanism
Crystallographic orientation-dependent sodiation degree

ABSTRACT

Todorokite-type manganese dioxide (τ-MnO_2) with large tunneled structure has been considered a promising electrode material used in sodium-ion batteries (SIBs) for large-scale energy storage systems. Precise understanding of sodium storage mechanisms in such large tunnels, however, still remains ambiguous due to a lack of direct atomic-level observation. Here, structural evolutions of τ-MnO_2 nanorods (NRs) mainly composed of specific 4×3 tunnels during (de)sodiation are studied carefully with *in-situ* transmission electron microscopy, including lattice-resolution imaging, consecutive electron diffraction, and electron energy loss spectroscopy, coupled with density functional theory calculations. By real-time tracing the full sodiation process, multistep phase conversion reactions are revealed, beginning with tunnel-based Na^+-intercalation, undergoing the formation of intermediate $Na_{0.25}MnO_2$ and $NaMnO_2$ phases as result of tunnel distortion and degradation, and ending with the final MnO phase. Furthermore, we witness the first lattice-level visualization of different sodiation degrees correlated with crystallography orientations under the same field of view, unveiling the anisotropic contraction and expansion of lattice *a* and *c* upon inserting Na^+ ions, as corroborated by density functional theory (DFT) calculations. During the following desodiation, the extraction of Na^+ ions causes the recolonization of the $NaMnO_2$ phase (rather than the original τ-MnO_2). Subsequently, a reversible and symmetric conversion reaction between MnO and $NaMnO_2$ phases is established upon the repeated (de)sodiation cycles. This work affords valuable insights into electrochemical sodium storage mechanisms of tunnel-structured τ-MnO_2 material, with the hope of assistance in designing SIBs with high-rate capability based on homogeneous tunnel-specific phase.

1. Introduction

For the emerging electric vehicles and power grid storage, concerns about limited natural abundance and uneven global distribution of lithium resources render the necessity to develop new battery systems other than lithium-ion batteries (LIBs) [1–4]. Alternatively, sodium-ion batteries (SIBs) have recently aroused much interest for large-scale energy storage in the applications of renewable energy and smart grid because of their low cost and infinite sodium resources [5–8]. However, finding suitable materials as electrodes is still challenging for SIBs, as Na^+ ion has a larger radius, that is, 55% larger than that of Li ion, and heavier mass, significantly impacting the ionic transport and reaction kinetics within electrodes [9]. Guided by the similar chemistry of Li, many mature electrode materials in LIBs have been transferred for use in SIBs, such as CuO, SnO_2, and MoO_3 [10–14]. In fact, only a part of such electrode materials used in LIBs are suitable for reversible (de)insertion reaction of Na^+ ions due to a higher diffusion barrier of Na^+ ions. As a result, understanding the relationship between the size of intercalating Na^+ ions and the dimensionality of ionic diffusion channels in the host crystal is prerequisite to find appropriate electrode materials.

Manganese dioxide (MnO_2) materials, known for the rich polymorphs with various open structures, have been widely researched as very promising electrode candidates for SIBs, due to their wide abundance, low cost, low toxicity, and high safety [15,16]. Currently, most of the reported MnO_2 cathodes possess a two-dimensional layered structure or small tunnel-type structure composed by edge-shared MnO_6

* Corresponding authors.
E-mail addresses: p-gao@pku.edu.cn (P. Gao), slt@seu.edu.cn (L. Sun), fxu@seu.edu.cn (F. Xu).
[1] These authors contributed equally to this work.

https://doi.org/10.1016/j.ensm.2021.02.023
Received 1 November 2020; Received in revised form 8 February 2021; Accepted 15 February 2021
Available online 17 February 2021

octahedra chains [17–23]. Such compact crystal structure with small internal tunnels accounts for quite sluggish kinetics of Na-ion diffusion, which in turn leads to a poor rate performance. Therefore, designing an open structure with larger diffusion tunnels and more accessible insertion sites is highly desired to develop advanced electrode materials for SIBs. In this regard, todorokite-type MnO_2 (τ-MnO_2) that has a larger open tunnel framework built by [MnO_6] octahedra forming quadrilateral tunnels of $p \times 3$ dimensions ($p \geq 3$) has attracted extensive attention [24–28]. Cations and water molecules locate in such tunnels and stabilize the large open crystallographic framework [29–32]. Previous studies have revealed that the Na^+ ions occupy preferentially larger tunnels and then diffuse within them owing to the lower diffusion barrier [33,34]. However, the transport kinetics of Na^+ ions in such tunnels and concomitant tunnel structure evolution still remain largely unknown. In particular, the dynamic response of tunnel-specific structures upon (de)sodiation cycle has not been investigated so far, leading to the lack of cognition on the underlying electrochemical sodium storage mechanisms of τ-MnO_2.

Here, τ-MnO_2 nanorods (NRs) mainly composed of specific 4×3 tunnels have been synthesized for the first time and identified by atomically resolved scanning transmission electron microscopy (STEM) imaging with a high-angle annular dark field (HAADF) detector. The electrochemical (de)sodiation behaviors of τ-MnO_2 NRs are subsequently studied with *in-situ* transmission electron microscopy (TEM), including lattice-resolution imaging, dynamic electron diffraction (ED), and electron energy loss spectroscopy (EELS), coupled with density functional theory (DFT) calculations. The ensemble of *in-situ* TEM techniques enable real-time tracking of ionic transport, electrochemical reactions, and solid-state phase transformations at single-nanorod level, affording an unprecedented opportunity to explore the Na storage mechanisms within tunnels of τ-MnO_2. The stepwise phase transformations during sodiation, involving the nucleation of a new $Na_{0.25}MnO_2$ phase followed by the formation of intermediate $NaMnO_2$ phase as a result of tunnel degradation, and the final MnO phase, are revealed. Particularly, under the same field of view in TEM observation, we witness for the first time the lattice-resolution visualization of different sodiation degrees dependent on crystallographic orientations, characterized by the anisotropic contraction and expansion of lattice *a* and *c*. Upon the first desodiation, we observed multiple extraction pathways of Na^+ ions and the sodiation products of MnO and Na_2O are converted back to $NaMnO_2$ phase, rather than the original τ-MnO_2 phase. Subsequently, a reversible and symmetric conversion reaction between MnO and $NaMnO_2$ phases can be established upon the repeated discharge-charge cycles. These details are in sharp contrast to the findings acquired during (de)lithiation of the τ-MnO_2 material. The present work reveals the precise sodiation mechanisms in the τ-MnO_2 material with specific 4×3 tunnels and provides valuable guidance to optimize the tunnel-structured electrode materials for SIBs with high-performance energy storage.

2. Experimental section

2.1. Materials preparation

The tunnel-structured τ-MnO_2 NRs were formed by autoclaving the high-quality precursor of layer-structure manganese oxides [27,29]. In brief, 50 mL of 0.5 M NaOH and 50 mL of 1 M H_2O_2 were mixed and then added to 50 mL of 0.3 M $Mn(NO_3)_2$ under stirring for 1 h. Afterwards, the precipitate of Na-birnessite manganese oxide was obtained by filtration and washing with deionized water. Then, the obtained Na-birnessite precipitate was transferred into 1 L of 1 M $MgCl_2$ solution for 48 h to fully replace Na^+ ions with Mg^{2+} ions. After filtration and washing, the obtained precipitate was dispersed again in another 1 L of 1 M $MgCl_2$ solution. The ion exchange process was repeated five times at least, enabling a complete phase transformation from Na-birnessite to Mg-buserite. Subsequently, 50 mg of Mg-buserite was filtered and then washed with distilled water, and re-dispersed in 17 mL of 1 M $MgCl_2$ solution. The mixture was transferred into a sealed Teflon-lined stainless autoclave and maintained at 220 °C for four days. The finally synthesized sample of τ-MnO_2 NRs was filtrated and washed with distilled water, and then dried in vacuum at 100 °C for 12 h.

2.2. Materials characterization

Phase structure and morphology of τ-MnO_2 were characterized by a powder X-ray diffractometer (XRD, ARLXTRA, Thermo Electron Co., USA) equipped a Cu Kα radiation source (λ = 0.15416 nm) operated at 40 kV and 30 mA with a scanning range of 2θ from 5 to 60° and a scanning electron microscope (SEM, JSM-7600F, JEOL, Japan) operated at 15 kV. Cross–section specimens of τ-MnO_2 NRs were prepared using a commercially available FIB system (SIM9200, Seiko Instrument Inc.) with a beam of 30 keV Ga^+ ions. Atomic-scale observation of side face of the NRs, electron diffraction (ED), electron energy loss spectroscopy (EELS), and energy dispersive X-ray spectroscopy were carried out using a double aberration-corrected FEI Titan Them G2 microscope operated at 300 kV. High-resolution scanning transmission electron microscopy (STEM) imaging was collected with a high-angle annular dark field (HAADF) detector. EELS data were recorded with a convergence angle of 21 mrad and a collection angle of 90 mrad. Atomically resolved STEM-HAADF imaging for the cross-section was conducted using a FEI Talos F200X TEM with an X-FEG electron source module operated at 200 keV.

2.3. In-situ *electrochemical sodiation/desodiation experiments*

The *in-situ* nano-battery was constructed in a high-resolution transmission electron microscope (FEI Tecnai F20, 200 kV) with a STM-TEM sample holder (Nanofactory Instruments and PicoFemto). The τ-MnO_2 NRs were attached to the Au rod by the conductive silver paste to ensure a good electrical contact. Bulk metal Na scraped onto tungsten (W) probe was used as the counter electrode and Na source. The holder was immediately transferred into the TEM column only with the exposure of s few seconds in air; thus, the naturally oxidized Na_2O layer during this transferring process acted as the solid electrolyte for the *in-situ* sodiation reaction. Afterwards, a constant −1.5 V/1.5 V potential was applied to a single NR with respect to the Na/Na_2O electrode to drive the Na^+ ions to insert into or extract from the NR, initiating the electrochemical sodiation and desodiation reactions.

2.4. DFT calculations

All DFT calculations were carried out by generalized gradient approximation (GGA) parameterized by the Perdew, Burke, and Ernzerhof (PBE) functional, as implemented in the Vienna Ab initio Simulation Package (VASP) [35-37]. The DFT + U corrections was applied to 3d orbitals of Mn [38-40]. Taking the magnetism of τ-MnO_2 into account, spin polarization was included in all DFT calculations. The Brillouin zone was sampled by 4 × 1 × 7 and the energy cutoff for the plane-wave basis set was 450 eV. The electronic iterations convergence criterion was set as 10^{-4} eV in energy and 0.01 eVÅ^{-1} in force. The initial structure of τ-MnO_2 includes twenty-eight manganese atoms with two large 4 × 3 intergrowth tunnels and two 1 × 1 tunnels. And it also includes 8 magnesium atoms and 16 water molecules within tunnels of the initial structure. The optimized parameters of τ-MnO_2 are a = 23.20 Å, b = 5.36 Å, and c = 9.14 Å, respectively.

2.5. Electrochemical measurements

The electrochemical performance of the as-synthesized τ-MnO_2 NRs was evaluated by the coin cells. Binder free self-supporting (BFSS) electrodes of τ-MnO_2 NRs, metallic sodium foils, and electrolyte were employed in the cells. The electrolyte in the Na half-cells was 1 M $NaClO_4$ in ethylene carbonate (EC)/dimethyl carbonate (DMC) (1:1, vol%) with

5% of fluoroethylene carbonate as the additive. Galvanostatic charge-discharge test was carried out at a current density of 0.1 A g^{-1} in the voltage range of 0.01–4 V using a multichannel battery testing system (LAND CT2001A). Cyclic voltammetry (CV) was tested in the voltage range of 0.01–3.0 V with a scan rate of 0.1 mV s^{-1}.

3. Results and discussion

The basic phase structure and chemical composition of as-synthesized τ-MnO_2 sample are firstly identified, Fig. S1 in Supplementary material. Power X-ray diffraction (XRD) analysis shows three dominant diffraction peaks at the 2θ of 9.2°, 18.5°, and 36.9° can be indexed as (001), (002), and (004) planes of monoclinic todorokite phase with high degree of crystallinity (space group *P*2/*m*, JCPDS #38–475) [24,27], as shown in Fig. S1a. The XRD result imply the good periodic lattice spacing along the *c*-axis orientation of crystal unit cell. Energy dispersive X-ray spectroscopy (EDS) mapping confirms three main elements of oxygen (O), manganese (Mn), and magnesium (Mg) with uniform distribution at single-nanoparticle level, Fig. S1b. Further EDS quantitative analysis shows that the sample has an atomic ratio of Mg:Mn being 0.29, corresponding to the chemical formula of $Mg_{0.29}MnO_2$, Fig. S1c. In general, magnesium exists in the form of hydrated cations in this structure, forming a structural formula of $Mg_{0.29}MnO_2{\cdot}0{\cdot}5H_2O$. A certain amount of hydrated Mg^{2+} cations can prevent the open tunnel framework of τ-MnO_2 from collapsing [29–32]. The low-magnification STEM-HAADF image and SEM image has found that the sample exhibits one-dimensional nanorod morphology with the cross-sectional dimension in the range of 20–50 nm and the length up to several tens of micrometers, because of which the nanorods tend to slightly bend and laterally aggregate with each other, Fig. S1d and Fig. S2. The average diametral dimension of these 1D nanorods estimated from XRD patterns using the Scherrer equation is in the range of 20–50 nm, also agreeing well with the TEM and SEM morphological observations. For the convenience of narration, $Mg_{0.29}MnO_2{\cdot}0{\cdot}5H_2O$ is hereinafter referred to as τ-MnO_2 all the time, unless otherwise specified.

The omnidirectional atomic-scale structural characterization for the lateral and axial directions of a single NR has been performed by aberration-corrected STEM-HAADF imaging. Fig. 1a,b show that the NR with a [010] growth direction is monocrystalline with a uniform diameter of about 45 nm. In Fig. 1c–e, the lateral STEM-HAADF image viewed along the [100] direction of a NR clearly shows its atomic structure, indicating three [MnO_6] octahedra along the *c*-axis orientation of crystal unit cell. Similarly, the HAADF-STEM image along the [001] direction confirms four [MnO_6] octahedra along the *a*-axis orientation, as shown in Fig. 1f–h. Referring to the atomic structure models, Mn atoms (indicated by blue dots) within the tunnels can be clearly discerned, but oxygen atoms (indicated by orange dots) are invisible in STEM-HAADF image due to its weak scattering power (lower atomic number). These STEM-HAADF characterizations along the *a* and *c* axes indicate the 4 × 3 tunnels within a NR, which is further corroborated by the cross-section observation viewed along the *b* axis of a NR (*i.e.*, the NR long axis parallels to the TEM electron beam), Fig. 1i–k. The magnified STEM-HAADF image along the [010] direction (or *b* axis) also confirms the 4 × 3 tunneled-structure, in which the bright spots surrounding each tunnel correspond to MnO_6 atomic columns, matching well with the atomic model structure viewed along the *b* axis in Fig. 1k. It can be seen from Fig. 1j that the columns of Mg^{2+} ions seem to loom up inside the 4 × 3 tunnels, but they are not definitely indicated, taking the current controversy in their position and number within the tunnels of τ-MnO_2 [33,41,42].

Despite our efforts to the controlled synthesis of the homogeneous tunnel-specific phase, we have to admit that no 100% pure 4 × 3 tunnels at single-nanorod level are achieved. Larger (6 × 3) or smaller (2 × 3) tunnels are also visible in the lower part of Fig. 1f and in the upper part of Fig. 1i, respectively. A recent work has reported that Mg^{2+}-stabilized

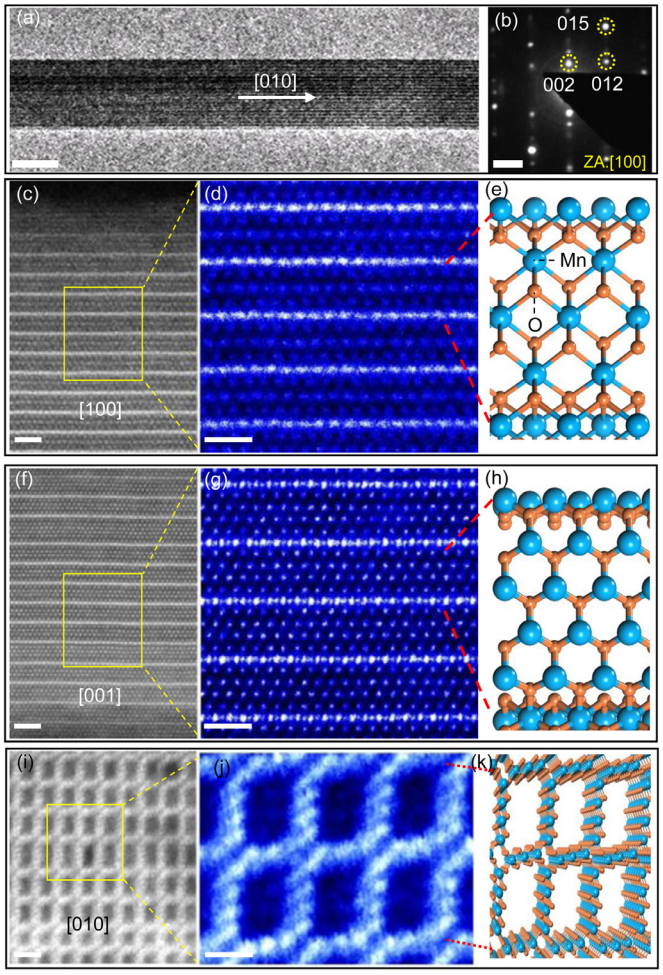

Fig. 1. (a) TEM image of a τ-MnO_2 NR (Scale bar, 30 nm) and (b) corresponding electron diffraction pattern (Scale bar, 5 1/nm). (c) The atomically resolved HAADF–STEM image viewed along the [100] direction. Scale bar, 2 nm. (d) The enlarged view of the reselected dark rectangle. Scale bar, 1 nm. (e) The corresponding atomic structure model. (f) The aberration-corrected HAADF-STEM image viewed along [001] zone axis. Scale bar, 2 nm. (g) The atomic resolution HAADF-STEM image of dark rectangle. Scale bar, 1 nm. (h) The atomic structure model which is well consistent with the HAADF-STEM image. (i) Cross-sectional HAADF-STEM image of τ-MnO_2 NR. Scale bar, 2 nm. (j) The atomically resolved HAADF-STEM image of an area in dark rectangle. Scale bar, 1 nm. (k) The atomic structure model viewed along the [010] axis. Blue and orange spheres are Mn and O atoms, respectively.

τ-MnO_2 todorokite should not be seen as a pure 3 × 3 tunneled structure but rather as a polytypic *p* × 3 tunnel family, where *p* is an integer generally less than or equal to 6, with 3 × 3, 4 × 3, and 5 × 3 tunnels appearing most frequently. For the polytypic *p* × 3 tunnel family, *p* is the variable but "3″ is usually stable. If it's true, this will well explain the reason why the periodic lattice spacing along the *a*-axis orientation of crystal unit cell cannot be reflected by the visible diffraction peak in the XRD pattern in Fig. S1a. Therefore, the phase purity of the as-synthesized 4 × 3 tunnel τ-MnO_2 needs to be further clarified. Based on the counting statistics of observing tens of atomically resolved STEM-HAADF images, the phase purity of the as-synthesized 4 × 3 tunnel τ-MnO_2 is determined to be ~92%, Fig. S3 and Table S1 in Supplementary material. Obviously, our observation and analyses of the sample at single-nanoparticle level and in bulk level conform to the regularity of *p* × 3 tunnel family.

To investigate electrochemical (de)sodiation behaviors of the τ-MnO_2 NRs, an all-solid nanosized SIB consisting of individual NRs was constructed in a TEM for *in-situ* electrochemical experiments, as

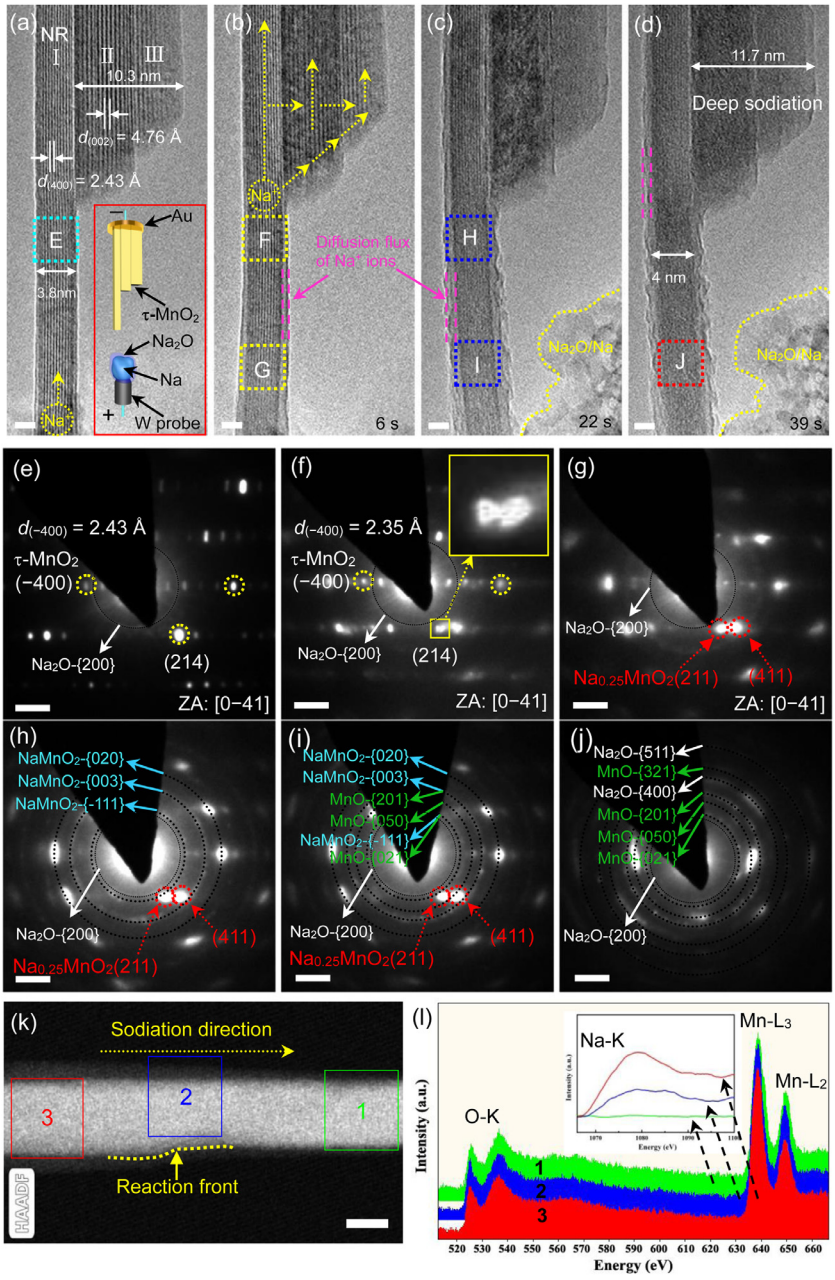

Fig. 2. (a–d) Snapshots of the first sodiation process from Movie S1. (a) HRTEM image of three attached τ-MnO_2 NRs. Inset is a schematic illustration of the all-solid nanoscale sodium-ion battery. (b) The early stage of sodiation. (c) Sodium ions coated the surface of NRsI, II and III. (d) The fully sodiated state. (a-d) Scale bars, 2 nm. (e) SAED pattern corresponds to the area marked as E in (a). (f–j) SAED patterns show the corresponding structural evolutions in (b)–(d), arrayed from low to high Na^+-content regions. (e-j) Scale bars, 5 1/nm. (k) STEM-HAADF image of a partially sodiated NR. Scale bar, 20 nm. (l) O K-, Mn L-, and Na K- edges recorded from the lcoations of 1, 2, and 3 labelled in k.

schematically illustrated by the inset in Fig. 2. Before sodiation, three pristine NRs (termed as NR I, II, and III) that were tightly overlapped laterally all show clear high-resolution lattice fringes, but only NR I directly contacted the Na source, Fig. 2a. Snapshots of the sodiation process of the three NRs from video are chronologically shown in Fig. 2b–d (see also Movie S1, Supplementary material). Upon applying a potential of −1.5 V to NR I with respect to the Na electrode, diffusion flux of Na^+ ions, characterized by a thin layer [43], firstly appeared on the surface of NR I and then propagated longitudinally, Fig. 2b. We can imagine that the Na^+ flux also diffused in like manner within tunnels of NR I along its long axial direction as reported previously [44], despite such a scenario is difficult to be visualized directly.

At 22 s in Fig. 2c, the Na^+ diffusion flux on the surface of NR I was transferred in succession to NRs II and III, triggering their sodiation reaction, as corroborated by the vanishing lattice fringes in NRs II and III (see also Movie S1, Supplementary material). Meanwhile, in addition to the moderate surface diffusion pathway, this transfer of Na^+ ions to adjacent NRs could also be fulfilled via a violent inter-NR mode characterized by across-tunnel diffusion, as observed previously in the example of 2 × 2 tunnel-structured α-MnO_2 NRs [22]. The observed ionic diffusion pathways can be schematically exhibited by the diagrams shown in Fig. S4. Unexpectedly, the firstly sodiated NR I still remained visible lattice fringes this moment, while the later sodiated NRs II and III already have no clear lattice fringes, as if the latter had faster sodiation kinetics compared with the former. Obviously, it seems unreasonable, because the latter was sodiated only by the Na resoure coming from the former that should have a higher degree of sodiation. Especially, upon a following full sodiation in Fig. 2d, NR I exhibited a radial expansion of only 5.2% (from 3.8 nm to 4.0 nm), which was much less than 13.6% (from 10.3 nm to 11.7 nm) of NRs II and III, further implying their different sodiation kinetics (as expatiated later). Despite such large size expansions, no fracture and cracks were observed for the deeply sodiated NRs, in sharp contrast to other oxide electrode materials without tunneled strucutres [12,45].

Structural and phase evolutions of individual τ-MnO_2 NRs during sodiation were tracked by consecutive electron diffraction (ED) patterns. Fig. 2e–j displays the corresponding ED patterns arrayed in the order of gradually increased Na^+ concentration on NR I. After the contact of the Na_2O electrolyte and NR I but before applying a negative potential, NR I shows the single-crystalline nature of τ-MnO_2 phase (JCPDS #38-475), as confirmed by the ED pattern (Fig. 2e) collected in the region E in Fig. 2a. During the process of the collection, the chemical sodiation would occur due to the fast tunnel-based diffusion of Na^+ ions; thus, a weak diffraction ring of Na_2O (200) plane also appears in the ED pattern. Soon after applying a negative potential, the ED pattern of the region F in Fig. 2b has indicated the beginning of intercalation reaction, Fig. 2f. Although the diffraction spots in the yellow circles (Fig. 2f) are nearly the same as those of the original state, implying well-preserved tunneled structure, the interplanar spacing of $(\bar{4}00)$ has undergone a slight spacing contraction from 2.43 Å to 2.35 Å, which may be caused by the strong interaction between the positively charged Na^+ ions and tunnel structure [46]. Despite this initial contraction, the interplanar spacing of $(\bar{4}00)$ basically tends to gradually expand due to the continued intercalation reaction, as observed by HRTEM in Fig. S5a–d in Supplementary material. The split of (214) diffraction spot was also observed, indicating the intercalation of foreign ions within tunnels. Afterwards, noticeable change with diffraction dots being elongated into circular arcs is observed, accompanied by the disappearance of the ED pattern of $(\bar{4}00)$ of the region G (Fig. 2g). Meanwhile, two diffraction spots corresponding to (211) and (411) planes of tetragonal $Na_{0.25}MnO_2$ phase (JCPDS #29-1244) emerge. Obviously, the emergence of new phases during sodiation is an important watershed that indicates the end of intercalation reaction and the beginning of conversion reaction. Note that the parent τ-MnO_2 phase is still preserved as evidenced by its remaining ED patterns along the $[0\bar{4}1]$ zone axis (Fig. 2g), implying some retention of the large tunnel framework available for ionic diffusion.

With further inserting Na^+ ions, the ED pattern of the parent τ-MnO_2 gradually became invisible (Fig. 2h), meaning that the tunneled structure had been seriously distorted. In addition to $Na_{0.25}MnO_2$ phase, the newly emerged diffraction rings (indicated by sky-blue arrows) show the formation of monoclinic $NaMnO_2$ phase (JCPDS #72-0830). Fig. 2i shows the ED pattern of heavily sodiated region I, characterized by the coexistence of orthorhombic MnO (JCPDS #04-0326) and monoclinic $NaMnO_2$ phases. It is worth noting that $Na_{0.25}MnO_2$ phase still existed at this stage. Fig. 2j shows the ED pattern of the fully sodiated region J in Fig. 2d and only the orthorhombic MnO phase and cubic Na_2O phase (JCPDS #03-1074) were found as the finally sodiated products, with the MnO phase embedded in the Na_2O matrix. Moreover, the ED patterns from metastable $Na_{0.25}MnO_2$ and $NaMnO_2$ phases vanished completely. These interplanar spacing values for identifying the various {*hkl*} planes are provided in Table S2 in Supplementary material. Therefore, we can infer that the τ-MnO_2 underwent multistep phase transformations from $Na_{0.25}MnO_2$ phase (upon the intercalation reaction) to $NaMnO_2$ phase, until the final MnO phase as a result of full sodiation.

To better verify the multistep phase evolutions during sodiation, electron energy loss spectroscopy (EELS) was collected along the Na^+ diffusion flux on a partially sodiated NR, Fig. 2k. Three locations marked by square frames on this NR were sampled, in which the location 2 is characterized by an obvious sodiation reaction front (RF) [22,43] as indicated by a yellow arrow, which provides the opportunity to analyze intermediate phases in the sodiating region. The location 3 behind the RF shows the deeply sodiated region, while the location 1 before the RF denotes a slight degree of sodiation (*i.e.*, the intercalation reaction) close to the pristine state. For each of the locations, EELS was sampled three times at least. Fig. 2l shows the constructed EELS profiles collected at these locations (Fig. 2k), in which Na K-edge, the pre-peak (K_α) of oxygen K edge, and Mn L_3 and L_2 white lines are indicated. From the spectra illustrated in Fig. 2l, we can find that the intensity of Na-K edge increases as the sodiation proceeds, clearly showing different degrees of sodiation on the respective regions.

EELS white-lines of Mn contain rich information about the density of unoccupied states near Fermi level and chemical bonding. In Fig. 2l, white-lines are pronounced, sharp peaks occurring near the onset of Mn $L_{2,3}$ edges, corresponding to electron transitions from $2p_{3/2}$ and $2p_{1/2}$ core states to bound unoccupied 3d states, respectively, which hybridize with oxygen 2p orbitals in Mn oxides. Each of the L_3 and L_2 peaks, separated by the spin-orbit interaction of the 2p core states, has its distinctive fine structure caused by atomic effects. Therefore, the ratio of integral white-line intensities of Mn $L_{3,2}$ has been used as the fingerprint to determine Mn valence [47–51]. Here the ratio of integral white-line intensities of Mn $L_{3,2}$ was calculated based on the Pearson method with double step functions [47,48], as detailed in Fig. S6a in Supplementary material. Taking the incorporation of hydrated Mg^{2+} cations into account, the initial valence state of Mn in pristine $Mg_{0.29}MnO_2$ should be approximately +3.5 instead of +4. From the calculated results in Fig. S6b, the white-line ratio increases from 2.35 (location 1) to 3.68 (location 3), corresponding to Mn oxidation states of +3.5 ($Mg_{0.29}MnO_2$) and +2 (MnO) [49], respectively. Additionally, the white-line ratio at location 2 was calculated to be around 2.6 that corresponds to Mn^{3+}, supporting the formation of intermediate $NaMnO_2$ phase [50]. By combining the EELS analyses and the aforesaid ED results, the sodiation process of τ-MnO_2 can basically be expressed by the following equation: $\tau\text{-}MnO_2 + 2Na^+ + 2e^- \rightarrow MnO + Na_2O$. Note that no metallic Mn is found for the whole sodiation process, which is different from the sodiation of other transition metal oxides such as ZnO and MoO_3, in which metallic phases are commonly formed due to the conversion reactions [13,45].

Fig. 3 further focuses on the comparison of sodiation kinetics at different crystallographic orientations of the three bundling NRs shown in Fig. 2. The bundling phenomenon of τ-MnO_2 NRs (see also SEM image in Fig. S2) with different crystallographic orientations should not be attributed to the widely accepted oriented attachment (OA) solution-grown of 1D nanostructures, this is because the OA mechanism tends to make the nanoparticles or nanorods spontaneously adjust to the same crystallographic orientations to form single-crystalline structure or alignment. Yuan et al. consider that the layer-to-tunnel mechanism should be responsible for this bundling, in which the layered Mg-birnessite precursors gradually split into laterally connected NRs due to the Mn migration/depletion at the crystal boundaries [52,53]. As shown in Fig. 2a, pristine NR I showed a well-resolved fringe spacing of 2.43 Å, corresponding to the (400) plane of τ-MnO_2, while NRs II and III had a lattice spacing of 4.76 Å, corresponding to the (002) plane. These NRs exposed different crystallographic orientations to the TEM imaging electron beam, which provides the opportunity to directly visualize the sodiation kinetics at different crystallographic orientations under the same field of view. Upon initial sodiation, the Na^+ ions firstly diffused inside/on the surface of NR I along its longitudinal direction and then gradually reached the contact regions between NRs I and II, where Na^+ ions were facilely tranferred laterally to NR II and then to NR III, initiating sodiation of the latter. As a result, the lattice fringes of (002) plane in NRs II and III were severely distorted and even collapsed after sodiation for 12 s, as displayed by the magnified image in Fig. 3b. On the contrary, well-resolved lattice fringes of (400) plane were still remained for NR I only with a slight expansion of ~2% in spite of a longer sodiation time, Fig. 3c. This has indicated the sodiation kinetics dependent on crystallographic orientations for a single τ-MnO_2 NR. In addition, after the deep sodiation in Fig. 2d, the radial expansion rate of NR I was much less than those of NRs II and III, further implying asymmetric crystal cell expansion along different crystallographic orientations of τ-MnO_2 NRs. Considering the fact that {400} planes are sensitive to the evolution of lattice *a*, while {002} planes reflect the change of lattice parameter *c*, such an asymmetric expansion likely originated from different response degrees of crystal unit cells along the [100] and [001] directions upon the insertion of Na^+ ions.

To further corroborate this conjecture, density functional theory (DFT) calculation was performed to better unravel local atomic struc-

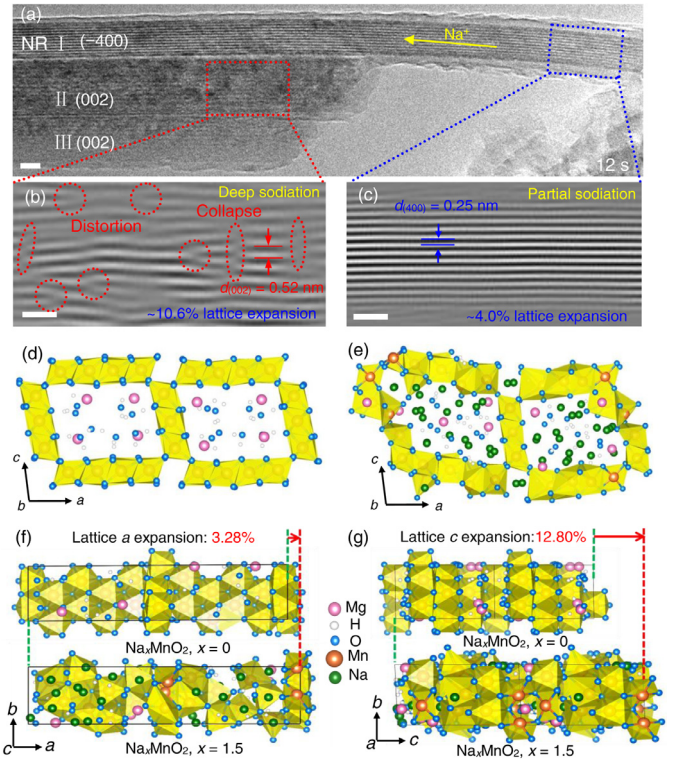

Fig. 3. (a) HRTEM image of a partially sodiated τ-MnO_2 NR. Three attached NRs (I, II and III). (b) Magnified HRTEM image of NR II (red rectangle). (c) Magnified HRTEM image of NR I (blue rectangle). Scale bar, 1 nm. (d) The intergrowth structure of two 4 × 3 tunnels along the *b* axis by using DFT calculations. (e) Stable atomic structure ($Na_{1.5}MnO_2$·phase) viewed along [010] zone axis. (f) and (g) $Na_{1.5}MnO_2$ phase viewed along [001] and [100] zone axes demonstrate asymmetric expansion of lattice *a* and *c* during sodiation. The top row shows the pristine τ-MnO_2 phase. The bottom row shows the $Na_{1.5}MnO_2$ phase. (f) Lattice *a* expansion: 3.28%. (g) Lattice *c* expansion: 12.8%.

tures associated with sodiation degrees. The intergrowth structure of two 4 × 3 tunnels along the *b* axis of τ-MnO_2 was modeled based on lattice constants of a = 23.20 Å, b = 5.36 Å, c = 9.14 Å, and β = 99.66° referring to a recent calculation work [42], Fig. 3d (see also Table S3, Supplementary material). For more precise analysis, the tunnel stabilizers such as Mg^{2+} and H_2O have been included in the unit cell ($Mg_8Mn_{28}O_{56}$·$16H_2O$), despite considerably heavy computational workload. Our DFT simulations have suggested that the center position in the tunnel is unfavorable for initial Na^+ insertion; instead, the sites near the tunnel walls provide the lowest binding energy for accommodating Na^+ ions, as demonstrated in Fig. S7, Supplementary material. Fig. 4 shows the predicted behavior of lattice parameters *a* and *c* as a function of insertion amount of Na^+ ions. Upon inserting 0.57 Na^+ ion per MnO_2 formula unit, both lattice parameters *a* and *c* exhibited slight contractions, due to the electrostatic repulsion between the inserted Na^+ ions and the stabilizers within tunnels. As one Na^+ ion per MnO_2 formula unit was inserted, the lattice *a* still remained a slight contraction of ~3%, but the lattice *c* expanded by ~2.5%, as shown in Fig. 4 and Table S2, Supplementary material. This process may be accompanied by Jahn-Teller distortion of MnO_6 octahedra only in one direction [19]. With further insertion of 1.5 Na^+ ions (Fig. 3e), the lattice *a* expanded by ~3.28%, while the lattice *c* exhibited a large elongation of ~12.8%, as illustrated in Fig. 3f,g. The DFT results clearly prove the asymmetric *a*-*c* plane expansion down to single-tunnel scale in τ-MnO_2, and well explains the aforesaid *in-situ* TEM observation theoretically.

Reversible extraction of Na^+ ions is prerequisite for practical application of τ-MnO_2 in the rechargeable SIBs. Thus, the desodiation behavior of τ-MnO_2 NRs along with the structural and phase evolutions

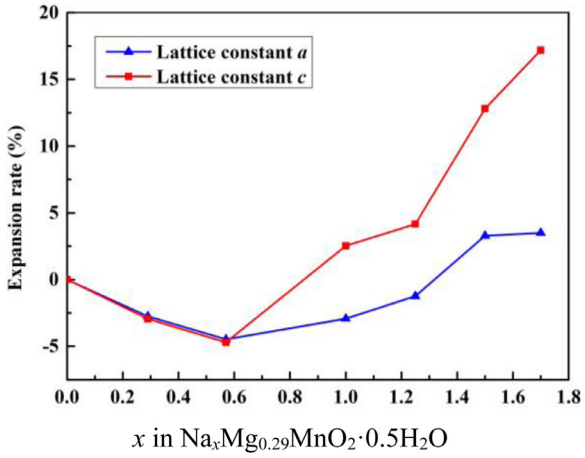

Fig. 4. Predicted behavior of lattice parameters *a* and *c* during sodium insertion.

were also investigated subsequently. Fig. 5 shows a series of TEM images of another two τ-MnO_2 NRs (NR A and B) upon desodiation (Movie S2, Supplementary material) and the corresponding sodiation process is also provided in Fig. S8 (Movie S3, Supplementary material). In Fig. 5a,b, the extraction of Na^+ ions directly led to the shrinkage of the NR A within 4 s. Although the NR B was not directly connected to Na electrode, Na^+ ions can still be extracted across the contact interface between NRs A and B, as denoted by white arrows, resulting in the desodiation of NR B. As the desodiation proceeded, both NRs A and B exhibited the distinct shrinkage in diameter from 18 nm to 14 nm and from 53 nm to 45 nm, respectively (Fig. 5c,d).

To track structural evolution during the desodiation of τ-MnO_2 NRs, the ED patterns were collected from NR B at different desodiation stages, as labeled by white dashed squares. Before desodiation, diffraction rings attributable to the (050), (201), and (321) planes of MnO phase (JCPDS #04-0326) and the (400) plane of Na_2O phase (JCPDS #03-1074) were detected, indicating the τ-MnO_2 was fully sodiated. Upon desodiation, the diffraction rings of Na_2O phase gradually vanished and the diffraction intensity of MnO phase decreased in Fig. 5f. In addition, another diffraction ring assigned to the (303) plane of $NaMnO_2$ phase (JCPDS #72-0830) occurred, suggesting the recolonization of $NaMnO_2$ phase. In the fully desodiated region (Fig. 5g), the ED patterns show the (002), (211), (411) and (611) planes of the monoclinic $NaMnO_2$ phase (JCPDS #72-0830), which indicates that the MnO phase was totally converted to the polycrystalline $NaMnO_2$ phase. Fig. 5h further displays the HRTEM image of the fully desodiated NR B and the ordered lattice fringes attributable to recrystallized $NaMnO_2$ were visible. To probe the valence changes of NR during desodiation, the EELS spectra of Na K-edge, the prepeak (K_α) of oxygen K edge, and Mn L_3/L_2 white lines were also acquired. In Fig. 5i, the intensity of Na-K edge gradually declined as the desodiation went on, indicating that Na^+ ions have been extracted. Note that some Na species still remained in NR even after a prolonged desodiation process, which accords with the formation of desodiated product of $NaMnO_2$. The valence state of Mn in NR before (red profile) and after (blue profile) desodiation was also analyzed in Fig. 5j. The ratio of white-line integral intensities of Mn $L_{3,2}$ has changed from ~3.7 to ~2.6 after a full desodiation, suggesting the transformation from Mn^{2+} to Mn^{3+}. By the combination of the ED and the EELS results, we can conclude that the MnO phase was converted back to $NaMnO_2$ phase upon desodiation, rather than the original τ-MnO_2 phase. Thus, the desodiation reaction can be expressed as the reaction: $MnO + Na_2O \rightarrow NaMnO_2$. Such an irreversible phase transformation is generally observed for transition metal oxides during their first (de)sodiation or (de)lithiation cycle, such as MoO_3, $NiCo_2O_4$, Fe_2O_3, and $ZnFe_2O_4$ [13,54–56].

To figure out the overall sodium storage mechanism, multi-cycle (de)sodiation processes of τ-MnO_2 NRs were subsequently investigated,

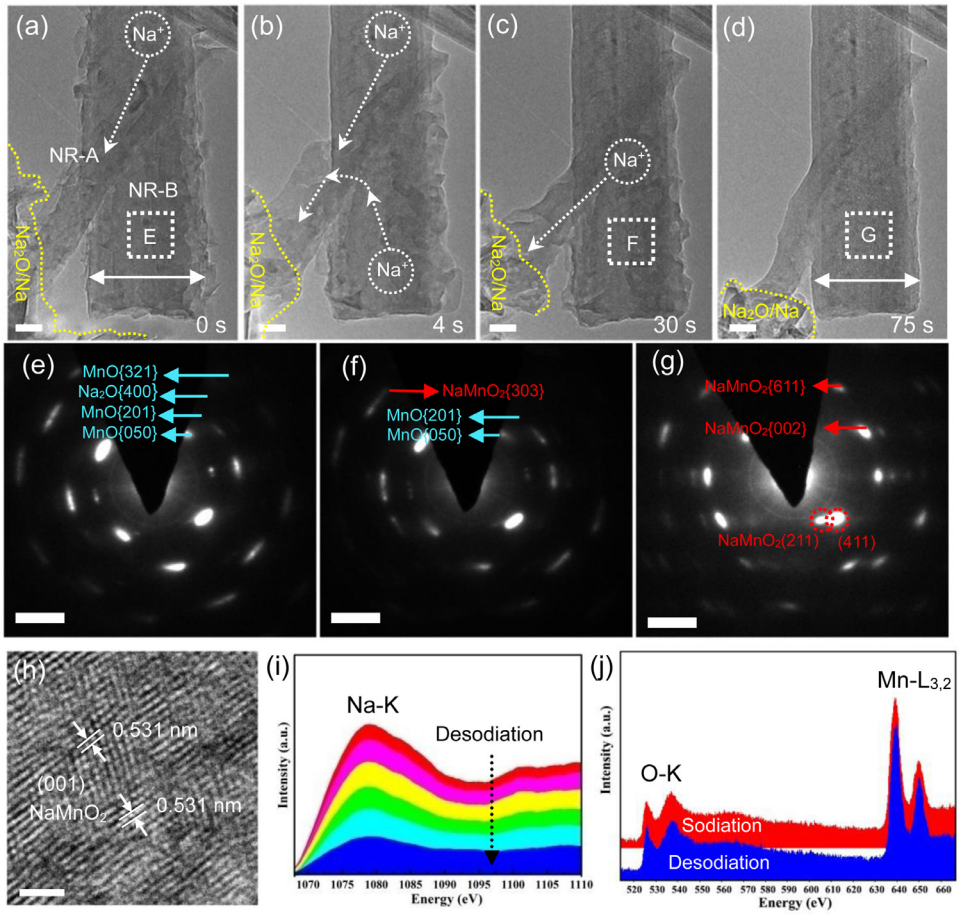

Fig. 5. (a–d) Snapshots of the desodiation process from Movie S3, showing the Na-extraction pathways. Scale bars, 10 nm. (a) Morphology of full sodiation NR A and B, in which NR B is not directly connected to the Na source. (b) Extraction of sodium ions leads to the shrinkage of the NR A. (c) The continuous desodiation of NRs A and B, because sodium ions can be extracted across the contact interface of adjacent τ-MnO_2 NRs. (d) The final desodiation state of NRs A and B. (e–g) SAED patterns collected from different desodiation stages of the NR B. Scale bars, 5 1/nm. (e) SAED pattern before desodiation. (f) SAED pattern of the heavy desodiation. (g) SAED pattern of the full desodiation. (h) HRTEM image of the desodiated NR B. Scale bar, 2 nm. (i–j) The EEL spectra of a partial desodiation NR. (i) Na K-edge. (j) O K- and Mn L-edges.

as shown in Fig. 6 (see also Movie S4, Supplementary material). Interestingly, the NR in Fig. 6a–g undergoing multicycle (de)sodiation can withstand repeated volume expansion and contraction, implying its good flexibility for electrode material of rechargeable SIBs. Fig. 6h further displays the radial expansion and contraction rates for each electrochemical sodiation-desodiation cycle. In particular, the radial expansion rate during the first sodiation is by far higher than those during the following sodiation, suggesting a higher degree of sodiation due to possibly different reaction mechanisms. Therefore, we have studied the ED patterns during the second sodiation-desodiation cycle carefully. It can be found from Fig. 6i,j that although the starting phases during the second sodiation was $NaMnO_2$, rather than τ-MnO_2 during the first sodiation, the sodiated products were the same, *i.e.*, MnO and Na_2O phases (Fig. 6k). Moreover, the ED patterns of desodiated products during the second desodiation was also the same as that of the first desodiated products (Fig. 6l). These findings indicate that the asymmetric phase transformation only took place during the first sodiation-desodiation, while the reversible and symmetric phase transformation between $NaMnO_2$ and MnO were subsequently established.

The electrochemical performance of SIBs based on τ-MnO_2 NRs was tested to delineate the sodiation mechanism of τ-MnO_2 material. In Fig. S9a, the cyclic voltammetry (CV) curves at a scan rate of 0.1 mV s^{-1} reflect the stepwise sodiation characteristic corresponding to three distinct reaction regions labeled as I, II, and III. For the region I of the first discharge process, the CV curve shows that the insertion of Na^+ ions occurs over a wide voltage range without intense cathodic peaks until ~1.5 V and the intercalation reaction should dominate this stage. By combining the aforesaid ED pattern and DFT calculations, it is considered that x in $Na_xMg_{0.29}MnO_2$ is around 0.25 for the limit of the intercalation reaction. Before inserting 0.25 Na^+ ion, the ED patterns (Fig. 2e,f) did not detect new phases. Another direct evidence is that the clear lattice fringes corresponding to tunnel walls of [MnO_6] octahedra are still preserved prior to the insertion of 0.25 Na, as observed in the region E and F in Fig. 2a,b. Following this intercalation stage, the deep sodiation characterized by multiple conversion reactions would take place in the region II involving the formation of intermediate $NaMnO_2$ phase and in the region III corresponding to the phase evolution from $NaMnO_2$ to MnO. A distinct cathodic peak at around 1.0 V may be associated with the formation of the $NaMnO_2$ phase and the breakage of the tunnels [21]. Afterwards, when fully discharged to 0.5 V, the MnO phase is formed and the valence state of Mn continuously decreases to about +2. Note that the area of the first CV curve is the largest, indicating that the first discharge-charge cycle has different sodiation reactions from those during the following cycles; while the following CV curves exhibit almost the same area, implying the reversibility and symmetry of phase transformations during the subsequent discharge-charge cycles. Fig. S9b shows the discharge-charge profile collected at a current rate of 0.1 A g^{-1} between 0.01 V and 3.0 V (vs. Na/Na^+), which also indicates the same multistep sodiation reactions (intercalation and conversion reactions) as those in Fig. S9a.

Last but not least, the presence of stabilizing Mg^{2+} cations inside the 4 × 3 tunnels should not be ignored, considering their effect on sodium storage property. Ref. [57] has revealed that a higher concentration of stabilizing K^+ ions can improve rate capability of α-MnO_2 material as the LIB cathode by both enlarging the 2 × 2 tunnels and enhancing the electron conductivity. However, the effect of tunnel cations on the electrochemistry is still controversial, because lowering the stabilizing ion concentration has also been proved by Takeuchi's group to improve the battery performance of tunneled α-MnO_2 nanostructures [58]. Such seemingly inconsistent results could also happen for Mg-

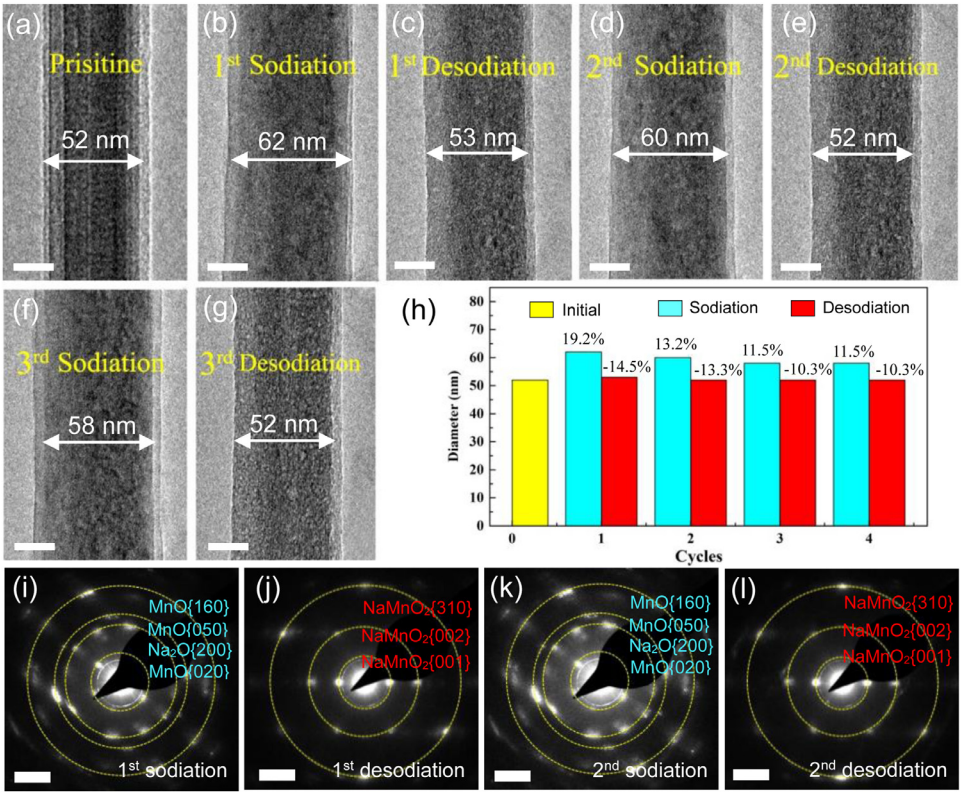

Fig. 6. (a–g) Microstructure evolutions of τ-MnO_2 NR during three sodiation-desodiation cycles. The NR exhibited multi-cycle reversible volume expansion and contraction with the insertion and extraction of sodium ions. Scale bars, 20 nm. (h) The measured diameters *versus* electrochemical cycling times of the τ-MnO_2 NR. (i–l) Electron diffraction patterns of the first and the second sodiation-desodiation cycle products for identifying the overall reaction mechanism of τ-MnO_2. The first fully sodiated products are MnO and Na_2O and the first delithiated product is $NaMnO_2$, consistent with the products of the second sodiation-desodiation cycle, indicating that reversible electrochemical reactions occurs between MnO and $NaMnO_2$ phases. Scale bars. 5 1/nm.

based todorokite-type MnO_2, considering the current inconsistence in understanding the position and number of the columns of Mg^{2+} ions inside the larger tunnels. For instance, Yuan et al. have obtained the number (n) of Mg^{2+} columns in the center of an $M \times N$ tunnel by a regularity: $n = (M - 2) \times (N - 2)$ with $M > 2$ and $N > 2$ [33]. Nonetheless, some atomic columns loom up near the tunnel sides and corners from figures in that work. Similar observation also appears in another recent report [41]. Furthermore, the DFT calculations definitely show that Mg^{2+} columns should locate near the corner of tunnels, rather than in the center [42]; if not so, the larger open tunnel framework of todotokite-type MnO_2 will become unstable. According to the DFT results, the 5 × 3 tunnels need 4 Mg^{2+} columns to stabilize the tunnel framework, in sharp contrast to 3 Mg^{2+} columns deduced by the aforesaid regularity. Therefore, further effort to clarifying the occupied position and number of Mg^{2+} columns inside the tunnels is necessary, as the stabilizing ions would affect the amount and position of inserted Na^{2+} ions, as illustrated by our preliminary DFT calculation in Fig. S7, Supplementary material. Despite the difficulty in real-time atomic-scale observation during the dynamic *in-situ* experiments, however, further visualization evidence showing how the tunnel ions affect Li^+/Na^{2+} ions storage is still expected.

4. Conclusion

In conclusion, the τ-MnO_2 NRs mainly composed of specific 4 × 3 tunnels have been synthesized and the electrochemical (de)sodiation mechanisms have been revealed by the *in-situ* TEM technique and DFT calculations. By virtue of the EELS and ED analyses, the τ-MnO_2 NRs were found to undergo multi-step phase transformations during sodiation process, *i.e.*, the τ-MnO_2 NRs were initially sodiated to $Na_{0.25}MnO_2$ phase upon the intercalation reaction and then converted into $NaMnO_2$ phase which was further sodiated to crystallized MnO nanograins embedded within the Na_2O matrix. In particular, we report the first lattice-resolution visualization of sodiation degrees at different crystallography orientations under the same field of view, revealing the anisotropic evolution of the lattice a and c, as corroborated by DFT calculations. Upon the succedent desodiation, the extraction of Na^+ ions led to the recolonization of the $NaMnO_2$ phase, rather than the original τ-MnO_2 phase. Subsequently, a reversible and symmetric transformation between MnO and $NaMnO_2$ phases was established during the following sodiation–desodiation cycles. This work affords mechanistic insights into electrochemical (de)sodiation of τ-MnO_2 material, different from findings during its (de)lithiation [59], with the hope of assistance in designing high-rate SIBs based on homogeneous tunnel-specific phase.

Credit author statement

F.X., R.C., and Y.W. synthesized the bulk material using a similar but modified method (Science, 1981, 212, 1024; RSC Advances, 2015, 5, 106265). F.X. and R.C. conducted all *in situ* experiments in Southeast University and Peking University, respectively. P.G., Y.S. and S.C. characterized the atomic structure of nanorod sides via scanning transmission electron microscopy with a high-angle annular dark field detector in Peking University. S.G., S.Z., and H.Z. completed density functional theory calculations. F.X., R.C., Y.W., P.G., and S.Z. carried out the data analysis. F.X. directed the whole work. All authors contributed to writing and revision of the manuscript.

Declaration of Competing Interest

The authors declare no competing financial interest.

Acknowledgments

This work was supported by the National Key Research & Development Program of China (grant no. 2020YFB2007400), the National Natural Science Foundation of China (grant nos. 51972058, 11774051, 61574034, 51372039, 21243011, 61674029, and 11902284), the National Basic Research Program of China (973 Program, grant no. 2015CB352106), and the Scientific Research Foundation of Graduate School of Southeast University (grant no. YBPY2026). The authors thank

Kisslinger Kim, Huolin Xin, and Shize Yang at Brookhaven National Laboratory for characterizing the cross-section of nanorod samples, and also thank Xiaobing Hu from Northwestern University and Li Zhong from Southeast University for useful discussion in writing and revising the manuscript. F.X., R.C., and Y.W. synthesized the bulk material using a similar but modified method (Science, 1981, 212, 1024; RSC Advances, 2015, 5, 106265). F.X. and R.C. conducted all *in-situ* experiments in Southeast University and Peking University, respectively. P.G., Y.S. and S.C. characterized the atomic structure of nanorod sides via scanning transmission electron microscopy with a high-angle annular dark field detector in Peking University. S.G. and S.Z. completed density functional theory calculations. F.X., R.C., Y.W., P.G., and S.Z. carried out the data analysis. F.X. directed the whole work. All authors contributed to writing and revision of the manuscript.

Supplementary materials

Supplementary material associated with this article can be found, in the online version, at doi:10.1016/j.ensm.2021.02.023.

References

[1] M. Armand, J.M. Tarascon, Nature 451 (2008) 652–657.
[2] X.L. Fan, E.Y. Hu, X. Ji, Y.Z. Zhu, F.D. Han, S. Hwang, J. Liu, S. Bak, Z.H. Ma, T. Gao, S. Liou, J.M. Bai, X. Yang, Y.F. Mo, K. Xu, D. Su, C.S. Wang, Nat. Commun. 9 (2018) 2324.
[3] M. Clites, J.L. Hart, M.L. Taheri, E. Pomerantseva, ACS Energy Lett 3 (2018) 562–567.
[4] R. Attias, M. Salama, B. Hirsch, Y. Goffer, D. Aurbach, Joule 3 (2018) 1–26.
[5] C. Wu, S.X. Dou, Y. Yu, Small 14 (2018) 1703671.
[6] J. Qin, T.S. Wang, D.Y. Liu, E.Z. Liu, N.Q. Zhao, C.S. Shi, F. He, L.Y. Ma, C.N. He, Adv. Mater. 30 (2018) 1704670.
[7] J. Pan, S.L. Chen, Q. Fu, Y.W. Sun, Y.C. Zhang, N. Lin, P. Gao, J. Yang, Y.T. Qian, ACS Nano 12 (2018) 12869–12878.
[8] H.H. Liu, H. Zheng, L. Li, S.F. Jia, S. Meng, F. Cao, Y.H. Lv, D.S. Zhao, J.B. Wang, Adv. Mater. Interface. 5 (2018) 1701255.
[9] Y.F. Yuan, K. Amine, J. Lu, R. Shahbazian-Yassar, Nat. Commun. 8 (2017) 15806.
[10] H.H. Liu, F. Cao, H. Zheng, H.P. Sheng, L. Li, S.J. Wu, C. Liu, J.B. Wang, Chem. Commun. 51 (2015) 10443–10446.
[11] Q.M. Su, G.H. Du, J. Zhang, Y.J. Zhong, B.S. Xu, Y.H. Yang, S. Neupane, W.Z. Li, ACS Nano 8 (2014) 3620–3627.
[12] M. Gu, A. Kushima, Y.Y. Shao, J.G. Zhang, J. Liu, N.D. Browning, J. Li, C.M. Wang, Nano Lett. 13 (2013) 5203–5211.
[13] W.W. Xia, F. Xu, C.Y. Zhu, H.L. Xin, Q.Y. Xu, P.P. Sun, L.T. Sun, Nano Energy 27 (2016) 447–456.
[14] S. Hariharan, K. Saravanan, P. Balaya, Electrochem. Commun. 31 (2013) 5–9.
[15] M. Maksud, N.K.R. Palapati, B.W. Byles, E. Pomerantseva, Y. Liu, A. Subramanian, Nanoscale 7 (2015) 17642–17648.
[16] S. Santhanagopalan, A. Balram, D.D. Meng, ACS Nano 7 (2013) 2114–2125.
[17] Y.L. Cao, L.F. Xiao, W. Wang, D. Choi, Z.M. Nie, J.G. Yu, L.V. Saraf, Z.G. Yang, J. Liu, Adv. Mater. 23 (2011) 3155–3160.
[18] X.B. Hu, J.P. Huang, L.J. Wu, M. Kaltak, M.V. Fernandez-Serra, Q.P. Meng, L. Wang, A.C. Marschilok, E.S. Takeuchi, K.J. Takeuchi, M.S. Hybertsen, Y.M. Zhu, Chem. Mater. 30 (2018) 6124–6133.
[19] Y.F. Yuan, A.M. Nie, G.M. Odegard, R. Xu, D.H. Zhou, S. Santhanagopalan, K. He, H. Asayesh-Ardakani, D.D. Meng, R.F. Klie, C. Johnson, J. Lu, R. Shahbazian-Yassar, Nano Lett. 15 (2015) 2998–3007.
[20] K.F. Chen, C.T. Sun, D.F. Xue, Phys. Chem. Chem. Phys. 17 (2015) 732–750.
[21] S. Lee, L.J. Wu, A.S. Poyraz, J.P. Huang, A.C. Marschilok, K.J. Takeuchi, E.S. Takeuchi, M. Kim, Y.M. Zhu, Adv. Mater. 29 (2017) 1703186.
[22] F. Xu, L.J. Wu, Q.P. Meng, M. Kaltak, J.P. Huang, J.L. Durham, M. Fernandez-Serra, L.T. Sun, A.C. Marschilok, E.S. Takeuchi, K.J. Takeuchi, M.S. Hybertsen, Y.M. Zhu, Nat. Commun. 8 (2017) 15400.
[23] J. Billaud, R.J. Clément, A.R. Armstrong, J. Canales-Vázquez, P. Rozier, C.P. Grey, P.G. Bruce, J. Am. Chem.Soc. 136 (2014) 17243–17248.
[24] S. Turner, P.R. Buseck, Science 212 (1981) 1024–1027.
[25] J. Lee, J.B. Ju, W.I. Cho, B.W. Cho, S.H. Oh, Electrochim. Acta 112 (2013) 138–143.
[26] B.W. Byles, P. West, D.A. Cullen, K.L. More, E. Pomerantseva, RSC Adv. 5 (2015) 106265–106271.
[27] B.W. Byles, D.A. Cullen, K.L. More, E. Pomerantseva, Nano Energy 44 (2018) 476–488.
[28] B.W. Byles, N.K.R. Palapati, A. Subramanian, E. Pomerantseva, APL Mater. 4 (2016) 046108.
[29] Y.F. Shen, R.P. Zerger, R.N. De Guzrnan, S.L. Suib, L. McCurdy, D.I. Potter, C.L. O'Young, Science 260 (1993) 511–515.
[30] J.E. Post, D.L. Bish, Am. Mineral. 73 (1988) 861–869.
[31] Q. Feng, H. Kanoh, Y. Miyai, K. Ooi, Chem. Mater. 7 (1995) 1722–1727.
[32] M.J. Duncan, F. Leroux, J.M. Corbett, L.F. Nazar, J. Electrochem. Soc. 145 (1998) 3746–3757.
[33] Y.F. Yuan, C. Liu, B.W. Byles, W.T. Yao, B.A. Song, M. Cheng, Z.N. Huang, K. Amine, E. Pomerantseva, R. Shahbazian-Yassar, J. Lu, Joule 3 (2019) 471–478.
[34] B.W. Byles, M. Clites, D.A. Cullen, K.L. More, E. Pomerantseva, Ionics (Kiel) 25 (2019) 493–502.
[35] J.P. Perdew, K. Burke, M. Ernzerhof, Phys. Rev. Lett. 78 (1997) 1396.
[36] G. Kresse, J. Hafner, Phys. Rev. B 47 (1993) 558–561.
[37] P.E. Blöchl, Phys. Rev. B 50 (1994) 17953.
[38] V.I. Anisimov, F. Aryasetiawan, A.I. Lichtenstein, J. Phys. Condens. Matter 9 (1997) 767–808.
[39] F. Zhou, M. Cococcioni, C.A. Marianetti, D. Morgan, G. Ceder, Phys. Rev. B 70 (2004) 235121.
[40] D.A. Tompsett, M.S. Islam, Chem. Mater. 25 (2013) 2515–2526.
[41] M.R.A. Shikder, M. Maksud, G. Vasudevamurthy, B.W. Byles, D.A. Cullen, K.L. More, E. Pomerantseva, A. Subramanian, Nanoscale Adv. 1 (2019) 357–366.
[42] X.B. Hu, D.A. Kitchaev, L.J. Wu, B.J. Zhang, Q.P. Meng, A.S. Poyraz, A.C. Marschilok, E.S. Takeuchi, K.J. Takeuchi, G. Ceder, Y.M. Zhu, J. Am. Chem. Soc. 140 (2018) 6961–6968.
[43] J.Y. Huang, L. Zhong, C.M. Wang, J.P. Sullivan, W. Xu, L.Q. Zhang, S.X. Mao, N.S. Hudak, X.H. Liu, A. Subramanian, H.Y. Fan, L. Qi, A. Kushima, J. Li, Science 330 (2010) 1515–1520.
[44] Y.F. Yuan, L. Ma, K. He, W.T. Yao, A.M. Nie, X.X. Bi, K. Amine, T.P. Wu, J. Lu, R. Shahbazian-Yassr, Nano Energy 19 (2016) 382–390.
[45] F. Xu, Z.R. Li, L.J. Wu, Q.P. Meng, H.L. Xin, J. Sun, B.H. Ge, L. Sun, Y.M. Zhu, Nano Energy 30 (2016) 771–779.
[46] Y. Wu, X.M. Xu, C.Y. Zhu, P.C. Liu, S.Z. Yang, H.L. Xin, R. Cai, L.B. Yao, M. Nie, S.Y. Lei, P. Gao, L.T. Sun, L.Q. Mai, F. Xu, ACS Energy Lett. 4 (2019) 2081–2090.
[47] D.H. Pearson, C.C. Ahn, B. Fultz, Phys. Rev. B 47 (1993) 8471–8478.
[48] T. Riedl, T. Gemming, K. Wetzig, Ultramicroscopy 106 (2006) 284–291.
[49] J.H. Rask, B.A. Miner, P.R. Buseck, Ultramicroscopy 21 (1987) 321–326.
[50] H.Y. Tan, J. Verbeeck, A. Abakumov, G.V. Tendeloo, Ultramicroscopy 116 (2012) 24–33.
[51] L.A.J. Garvie, A.J. Craven, Phys. Chem. Miner. 21 (1994) 191–206.
[52] Y.F. Yuan, S.M. Wood, He K, W.T. Yao, D. Tompsett, J. Lu, A.M. Nie, M.S. Islam, R. Sha hbazian-Yassar, ACS Nano 10 (2016) 539–548.
[53] Y.F. Yuan, K. He, B.W. Byles, C. Liu, K. Amine, J. Lu, E. Pomerantseva, R. Shahbazian-Yassar, Chem 5 (2019) 1793–1805.
[54] C.Y. Zhu, F. Xu, H.H. Min, Y. Huang, W.W. Xia, Y.T. Wang, Q.Y. Xu, P. Gao, L.T. Sun, Adv. Funct. Mater. 27 (2017) 1606163.
[55] Q.M. Su, D. Xie, J. Zhang, G.H. Du, B.S. Xu, ACS Nano 7 (2013) 9115–9121.
[56] Q.M. Su, S.X. Wang, L.B. Yao, H.J. Li, G.H. Du, H.Q. Ye, Y.Z. Fang, Sci. Rep. 6 (2016) 28197.
[57] Y.F. Yuan, C. Zhan, K. He, H. Chen, W.T. Yao, S. Sharifi-Asl, B.A. Song, Z.Z. Yang, A.M. Nie, X.Y. Luo, H. Wang, S.M. Wood, K. Amine, M.S. Islam, J. Lu, R. Shahbazian-Yassar, Nat. Commun. 7 (2016) 13374.
[58] A.S. Poyraz, J. Huang, C.J. Pelliccione, X. Tong, S. Cheng, L. Wu, Y. Zhu, A.C. Marschiilok, K.J. Takeuchi, E.S. Takeuchi, J. Mater. Chem. A 5 (2017) 16914–16928.
[59] R. Cai, S.Y. Guo, Q.P. Meng, S.Z. Yang, H.L. Xin, X.B. Hu, M.Q. Li, Y.W. Sun, P. Gao, S.L. Zhang, H. Dong, S.Y. Lei, K. Kim, H.B. Zeng, L.T. Sun, F. Xu, Y.M. Zhu, Nano Energy 63 (2019) 103840.